

# A DEEP LEARNING BASED PIPELINE FOR EFFICIENT ORAL CANCER SCREENING ON WHOLE SLIDE IMAGES

Jiahao Lu\*, Nataa Sladoje\*, Christina Runow Stark<sup>§</sup>,  
Eva Darai Ramqvist<sup>‡</sup>, Jan-Michal Hirsch<sup>¶</sup>, Joakim Lindblad\*

\*Centre for Image Analysis, Dept. of Information Technology, Uppsala University, Sweden

<sup>§</sup>Dept. of Orofacial Medicine at Sdersjukhuset, Folkandvrden Stockholms Ln AB, Sweden

<sup>‡</sup>Karolinska Universitetsjukhuset, Dept. of Clinical Pathology and Cytology, Stockholm, Sweden

<sup>¶</sup>Department of Surgical sciences, Uppsala University, Sweden

## ABSTRACT

Oral cancer incidence is rapidly increasing worldwide. The most important determinant factor in cancer survival is early diagnosis. To facilitate large scale screening, we propose a fully automated end-to-end pipeline for oral cancer screening on whole slide cytology images. The pipeline consists of regression based nucleus detection, followed by per cell focus selection, and CNN based classification. We demonstrate that the pipeline provides fast and efficient cancer classification of whole slide cytology images, improving over previous results. The complete source code is made available as open source<sup>1</sup>.

**Index Terms**— CNN, Whole slide imaging, Big data, Cytology, Detection, Focus selection, Classification

## 1. INTRODUCTION

Cancer of the oral cavity is one of the most common malignancies in the world [1]. Similar to cervical cancer, visual inspection of brush collected samples has shown to be a practical and effective approach for early diagnosis and reduced mortality [2]. We, therefore, advocate for introducing screening of high risk patients in General Dental Practice by dentists and dental hygienists. Computer assisted cytological examination is essential for feasibility of this project, due to large data and high involved costs, [3].

Whole slide imaging (WSI) refers to scanning of conventional glass slides to produce digital slides. WSI is gaining popularity by pathologists worldwide, due to its potential to improve diagnostic accuracy, increase workflow efficiency, and improve integration of images with information systems [4]. Due to the large amount of data produced by WSI, manipulation and analysis are challenging and require special techniques. In spite of these challenges, advantage to reproduce the traditional light microscopy experience in digital format makes WSI a very appealing choice.

Deep learning (DL) has shown to perform very well in cancer classification. An important advantage, compared to (classic) model-based approaches, is absence of need for nucleus segmentation, a difficult task typically required for subsequent feature extraction. At the same time, the large amount of data provided by WSI makes DL a natural and favorable choice. In this paper we present a DL based segmentation-free pipeline for oral cancer screening on WSI.

## 2. BACKGROUND AND RELATED WORK

A number of studies suggest to use DL for classification of histology WSI samples, [5–9]. A common approach is to split tissue WSIs into smaller patches and perform analysis on the patch level. However, cytological samples are different from tissue; the natural unit of examination is the cell.

**Cell detection:** Many DL based nucleus detection methods are similar to the framework summarized in [10]: first generate a probability map by sliding a binary patch classifier over the whole image, then find nuclei positions as local maxima. However, considering that WSIs are as large as 10 giga-pixels, this approach is prohibitively slow. U-net models avoid the sliding window and reduce computation time. Detection is performed as segmentation where each nucleus is marked as a binary disk [11]. However, when images are noisy and with densely packed nuclei, the binary output mask is not ideal for further processing. We find the regression approach [12–14], where the network is trained to reproduce fuzzy nuclei markers, to be more appropriate.

**Focus selection:** Slide scanners do not provide sufficiently good focus for cytological samples and a focus selection step is needed. Building on the approaches of Just Noticeable Blur (JNB) [15] and Cumulative Probability of Blur Detection (CPBD) [16], Edge Model based Blur Metric (EMBM) [17] provides a no-reference blur metric by using a parametric edge model to detect and describe edges with both contrast and width information. It claims to achieve comparable results to the former while being faster.

This work is supported by: Swedish Research Council proj. 2015-05878 and 2017-04385, VINNOVA grant 2017-02447, FTV Stockholms Ln AB

<sup>1</sup><https://github.com/MIDA-group/OralScreen>

**Classification:** Convolutional Neural Networks (CNNs) have shown ability to differentiate healthy and malignant cell samples, [18]. Whereas the approach in [18] relies on manually selected free lying cells, our study proposes to use automatic cell detection. This allows improved performance by scaling up the available data to *all* free lying cells in each sample.

### 3. MATERIAL AND METHODS

#### 3.1. Data

Three sets of images of oral brush samples are used in this study. **Dataset 1** is a relatively small Pap smear dataset imaged with a standard microscope. **Dataset 2** consist of WSIs of the same glass slides as Dataset 1. **Dataset 3** consist of WSIs of liquid-based (LBC) prepared slides. All samples are collected at Dept. of Orofacial Medicine, Folktdandvrdn Stockholms ln AB. From each patient, samples were collected with a brush scraped at areas of interest in the oral cavity. Each scrape was either smeared onto a glass (Datasets 1 and 2) or placed in a liquid vial (Dataset 3). All samples were stained with standard Papanicolau stain. Dataset 3 was prepared with Hologic T5 ThinPrep Equipment and standard non-gynecologic protocol. **Dataset 1** was imaged with an Olympus BX51 bright-field microscope with a  $20\times$ , 0.75 NA lens giving a pixel size of  $0.32\ \mu\text{m}$ . From 10 Pap smears (10 patients), free lying cells (same as in ‘‘Oral Dataset 1’’ in [18]) are manually selected and  $80\times 80\times 1$  grayscale patches are extracted, each with one centered in-focus cell nucleus. **Dataset 2:** The same 10 slides as in Dataset 1 were imaged using a NanoZoomer S60 Digital slide scanner,  $20\times$ , 0.75 NA objective, at 11 z-offsets ( $\pm 2\ \mu\text{m}$ , step-size  $0.4\ \mu\text{m}$ ) providing RGB WSIs of size  $103936\times 107520\times 3$ ,  $0.23\ \mu\text{m}/\text{pixel}$ . **Dataset 3** was obtained in the same way as Dataset 2, but from 12 LBC slides from 12 other patients.

#### 3.2. Nucleus Detection

The nucleus detection step aims to efficiently detect each individual cell nucleus in WSIs. The detection is based on the Fully Convolutional Regression Networks (FCRN) approach proposed in [12] for cell counting. The main steps of the method are described below, and illustrated on an example image from Dataset 3, Fig. 1.

**Training:** Input is a set of RGB images  $I_i$ , and corresponding binary annotation masks  $B_i, i = 1 \dots K$ , where each individual nucleus is indicated by one centrally located pixel.

Each ground truth mask is dilated by a disk of radius  $r$  [11], followed by convolution with a 2D Gaussian filter of width  $\sigma$ . By this, a fuzzy ground truth is generated (Fig. 1b). A fully convolutional network is trained to learn a mapping between the original image  $I$  (Fig. 1a) and the corresponding ‘‘fuzzy ground truth’’,  $D$  (Fig. 1b). The network follows the architecture of U-Net [19].

**Inference:** A corresponding density map  $D'$  (Fig. 1c) is generated (predicted) for any given test image  $I$ . The density map

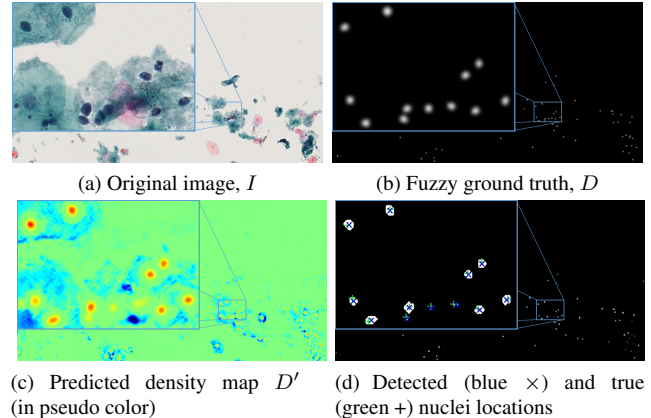


**Fig. 1:** A sample image at different stages of nucleus detection

$D'$  is thresholded at a level  $T$  and centroids of the resulting blobs indicate detected nuclei locations (Fig. 1d).

#### 3.3. Focus Selection

The focus level has to be selected for each nucleus individually, since different cells are at different depth. Standard tools (e.g., the microscope auto-focus) fail since they often focus on clumps or other artefacts. Our proposed method utilizes a number of equidistant z-levels acquired of the same specimen. Traversing the z-levels, the change between consecutive images shows the largest variance at the point where the specimen moves in/out of focus. This approach provides a clear improvement over solely relying on EMBM [17].

Following the Nucleus detection step we cut out a square region for each detected nucleus at all acquired focus levels. Each such cutout image is filtered with a median filter of size  $m\times m$  on each color channel to reduce noise. This gives us a set of smoothed images  $P_i, i = 1, \dots, N$ , of an individual nucleus at  $N$  consecutive z-levels. We compute the difference of neighboring focus levels,  $P'_i = P_{i+1} - P_i, i = 1, \dots, N-1$ . The variance,  $\sigma_i^2$ , is computed for each difference image  $P'_i$ :

$$\sigma_i^2 = \frac{1}{M} \sum_{j=1}^M (p'_{ij} - \mu_i)^2, \text{ where } \mu_i = \frac{1}{M} \sum_{j=1}^M p'_{ij},$$

$M$  is the number of pixels in  $P'_i$ , and  $p'_{ij}$  is the value of pixel  $j$  in  $P'_i$ . Finally the level  $l$  corresponding to the largest  $\sigma_i^2$  is selected. To determine which of the two images in the pair  $P'_i$  is in best focus, we use the EMBM method [17] as a post selection step to choose which of images  $P_l$  and  $P_{l+1}$  to use.

#### 3.4. Classification

The final module of the pipeline is classification of the generated nucleus patches into two classes – cancer and healthy. Following recommendation from [18], ResNet50 architecture [20] is used as a classifier in this pipeline.

The color information in this type of images is known to be less reliable than nucleus texture; we observe improved performance when relying on grayscale data compared to

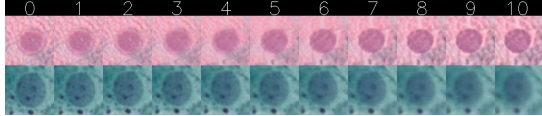


Fig. 2: Example of focus sequences for experts to annotate

when using the full RGB information. Therefore we convert the images to grayscale,  $L = 0.299R + 0.587G + 0.114B$ .

Considering that texture information is the key feature for classification [21], the data is augmented without interpolation. Throughout training, each sample is reflected with 50% probability and rotated by a random integer multiple of  $90^\circ$ .

## 4. EXPERIMENTAL SETUP

### 4.1. Nucleus Detection

Each WSI is split into an array of  $6496 \times 3360 \times 3$  sub-images [22]. The model is trained on 12 and tested on 2 sub-images (1014 resp. 119 nuclei). The manually marked ground truth is dilated by a disk of radius  $r = 15$ . All images, including ground truth masks, are resized to  $1024 \times 512$  pixels, using area weighted interpolation. A Gaussian filter,  $\sigma = 1$ , is applied to each ground truth mask providing the fuzzy ground truth  $D$ .

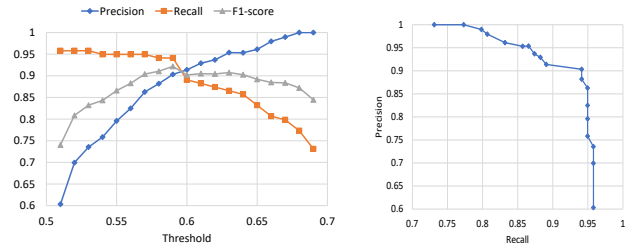
Each image is normalized by subtracting the mean and dividing by the standard deviation of the training set. Images are augmented by random rotation in the range  $\pm 30^\circ$ , random horizontal and vertical shift within 30% of the total scale, random zoom within the range of 30% of the total size, and random horizontal and vertical flips. Nucleus detection does not need the texture details, so interpolation does not harm. To improve stability of training, batch normalization [23] is added before each activation layer. Training is performed using RMSprop with mean squared error as loss function, learning rate  $\alpha = 0.001$  and decay rate  $\rho = 0.9$ . The model is trained with mini-batch size 1 for 100 epochs, the checkpoint with minimum training loss is used for testing.

Performance of nucleus detection is evaluated on Dataset 3. A detection is considered correct if its closest ground truth nucleus is within the cropped patch *and* that ground truth nucleus has no closer detections (s.t. one true nucleus is paired with at most one detection).

### 4.2. Focus Selection

100 detected nuclei are randomly chosen from the two test sub-images (Dataset 3). Every nucleus is cut to an  $80 \times 80 \times 3$  patch for each of 11 z-levels. For EMBM method the contrast threshold of a salient edge is set to  $c_T = 8$ , following [17].

To evaluate the focus selection, 8 experts are asked to choose the best of the 11 focus-levels for each of the 100 nuclei (Fig. 2). The median of the 8 assigned labels is used as true best focus,  $l_{GT}$ . A predicted focus level  $l$  is considered accurate enough if  $l \in [l_{GT} - 2, l_{GT} + 2]$ .



(a) Performance for different thresholds  $T$  (b) Precision-recall curve

Fig. 3: Results of nucleus detection

### 4.3. Classification

The classification model is evaluated on Dataset 1 as a benchmark, and then on Dataset 2, to evaluate effectiveness of the nucleus detection and focus selection modules in comparison with the performance on Dataset 1. The model is also run on Dataset 3 to validate generality of the pipeline. Datasets are split on a patient level; no cell from the same patient exists in both training and test sets. On Dataset 1 and 2, three-fold validation is used, following [18]. On Dataset 3, two-fold validation is used. Some cells in Dataset 2 and 3 lie outside the  $\pm 2 \mu\text{m}$  imaged z-levels, and the best focus is still rather blurred. We use the EMBM to exclude the most blurred ones. Cell patches with an EMBM score  $< 0.03$  are removed, leaving 68509 cells for Dataset 2 and 130521 for Dataset 3.

Slide level annotation and reliance on Malignancy associated changes (MAC) appears as a useful way to avoid need for large scale manual cell level annotations. Both [21] and [18] demonstrate promising results for MAC detection in histology and cytology. In our work, all cells from a patient with diagnosed oral cancer are therefore labeled as cancer.

We use Adam optimizer, cross-entropy loss and parameters as suggested in [24]. 10% of the training set is randomly chosen as validation set. Models are trained with mini-batch size 512 for 100 epochs on Dataset 2 and 3, and with mini-batch size 128 for 30 epochs on Dataset 1, since it contains fewer samples. When the validation loss has not decreased for 5 epochs, the learning rate is scaled by 0.1. Training is stopped after 15 epochs of no improvement. The checkpoint with minimum validation loss is saved for testing.

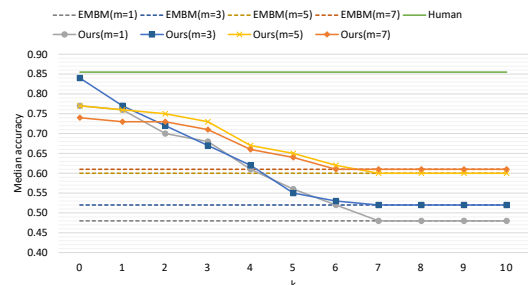
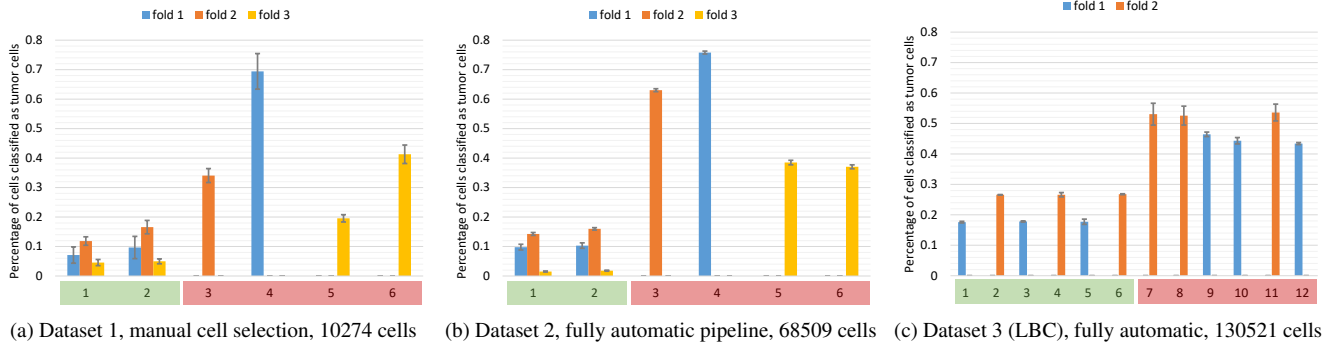


Fig. 4: Accuracy of focus selection



**Fig. 5:** Cell classification results per microscope slide; green samples are healthy, red samples are from cancer patients

## 5. RESULTS AND DISCUSSION

### 5.1. Nucleus Detection

Results of nucleus detection are presented in Fig. 3. Fig. 3a shows Precision, Recall, and F1-score as the detection threshold  $T$  is varied in  $[0.51, 0.69]$ . At  $T = 0.59$ , F1-score reaches 0.92, with Precision and Recall being 0.90 and 0.94 respectively. Precision reaches 1.00 for  $T = 0.68$ , with Recall being 0.77, as shown in Fig. 3b. Using  $T = 0.59$ , 94685 free lying nuclei are detected in Dataset 2 and 138196 in Dataset 3.

The inference takes 0.17 s to generate a density map  $D'$  of size  $1024 \times 512$  on an NVIDIA GeForce GTX 1060 Max-Q. In comparison, to generate a density map of the same size based on the sliding window approach (Table 4 of [10]), takes 504 s.

### 5.2. Focus Selection

Performance of the focus selection is presented in Fig. 4. The “human” performance is the average of the experts, using a leave-one-out approach. We plot performance when using EMBM to select among the  $2(k+1)$  levels closest to our selected pair  $l$ ; for increasing  $k$  the method approaches EMBM.

It can be seen that EMBM alone does not achieve satisfying performance on this task. Applying a median filter improves the performance somewhat. Our proposed method performs very well on the data and is essentially at the level of a human expert using  $k = 0$  and a  $3 \times 3$  median filter.

### 5.3. Classification

Classification performance is presented in Table 1 and Fig. 5. Results on Dataset 2 are better than on Dataset 1. This confirms effectiveness of the nucleus detection and focus selection modules; by using more nuclei (from the same samples) than those manually selected, improved performance is achieved. The results on Dataset 3 indicate that the pipeline generalizes well to liquid-based images.

In Fig. 6 we plot how classification performance decreases when nuclei are intentionally selected  $n$  focus levels away from the detected best focus. The drop in performance as we move away from the detected focus confirms the usefulness of the focus selection step.

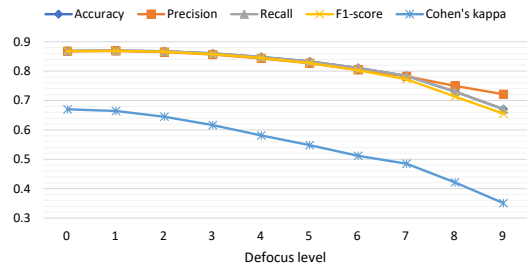


**Fig. 6:** The impact of defocused testset on fold 1, Dataset 2

**Table 1:** Classification performance

Dataset	Fold	Accuracy	Precision	Recall	F1-score
1	1	85.4±1.0	85.4±0.8	85.4±1.0	85.2±0.6
	2	79.5±1.6	82.2±0.3	79.5±1.6	80.7±0.9
	3	60.6±0.8	71.9±0.7	60.6±0.8	56.1±1.4
2	1	86.5±0.5	86.6±0.4	86.5±0.5	86.5±0.5
	2	80.4±0.6	82.1±0.4	80.4±0.6	81.1±0.5
	3	62.9±0.5	78.6±0.3	62.9±0.5	60.3±0.7
3	1	68.7±0.3	67.6±0.3	68.7±0.3	67.5±0.3
	2	67.5±1.2	68.7±1.4	67.5±1.2	68.0±1.2

If aggregating the cell classifications over whole microscopy slides, as show in Fig. 5, we observe that global thresholds can be found which accurately separate the two classes of patients in all the three observed datasets.

## 6. CONCLUSION

This work presents an automated end-to-end pipeline for oral cancer screening on whole slide images; source code is shared as open source. The proposed focus selection method performs at the level of a human expert and significantly outperforms EMBM. The pipeline can provide fully automatic inference for WSIs within reasonable computation time. It performs well for smears as well as liquid-based slides.

Comparing the performance on Dataset 1, using human selected nuclei and Dataset 2, using computer selected nuclei from the same microscopy slides, we conclude that the presented pipeline can reduce human workload while at the same time make the classification easier and more reliable.

## 7. REFERENCES

- [1] B.W.K.P. Stewart, Christopher P. Wild, et al., “World cancer report 2014,” *Public Health*, 2019.
- [2] R. Sankaranarayanan et al., “Long term effect of visual screening on oral cancer incidence and mortality in a randomized trial in Kerala, India,” *Oral Oncology*, vol. 49, no. 4, pp. 314–321, Apr. 2013.
- [3] P.M. Speight et al., “Screening for oral cancer—a perspective from the Global Oral Cancer Forum,” *Oral Surgery, Oral Medicine, Oral Pathology and Oral Radiology*, vol. 123, no. 6, pp. 680–687, June 2017.
- [4] N. Farahani, A.V. Parwani, and L. Pantanowitz, “Whole slide imaging in pathology: advantages, limitations, and emerging perspectives,” *Pathol Lab Med Int*, vol. 7, pp. 23–33, 2015.
- [5] G. Campanella et al., “Clinical-grade computational pathology using weakly supervised deep learning on whole slide images,” *Nature Medicine*, vol. 25, no. 8, pp. 1301–1309, Aug. 2019.
- [6] A. Cruz-Roa et al., “Accurate and reproducible invasive breast cancer detection in whole-slide images: A Deep Learning approach for quantifying tumor extent,” *Scientific Reports*, vol. 7, pp. 46450, Apr. 2017.
- [7] B. Korbar et al., “Deep Learning for Classification of Colorectal Polyps on Whole-slide Images,” *Journal of Pathology Informatics*, vol. 8, July 2017.
- [8] A. Teramoto et al., “Automated classification of benign and malignant cells from lung cytological images using deep convolutional neural network,” *Informatics in Medicine Unlocked*, vol. 16, pp. 100205, Jan. 2019.
- [9] K. Kiran GV and G. Meghana Reddy, “Automatic classification of whole slide pap smear images using CNN with PCA based feature interpretation,” in *Proc. of the IEEE Conf. on CVPR Workshops*, 2019.
- [10] H. Höfener, A. Homeyer, N. Weiss, J. Molin, C.F. Lundström, and H.K. Hahn, “Deep learning nuclei detection: A simple approach can deliver state-of-the-art results,” *Computerized Medical Imaging and Graphics*, vol. 70, pp. 43–52, Dec. 2018.
- [11] T. Falk et al., “U-Net: Deep learning for cell counting, detection, and morphometry,” *Nature Methods*, vol. 16, no. 1, pp. 67–70, Jan. 2019.
- [12] W. Xie, J.A. Noble, and A. Zisserman, “Microscopy cell counting and detection with fully convolutional regression networks,” *Computer Methods in Biomechanics and Biomedical Engineering: Imaging & Visualization*, vol. 6, no. 3, pp. 283–292, May 2018.
- [13] P. Kainz, M. Urschler, S. Schuler, P. Wohlhart, and V. Lepetit, “You Should Use Regression to Detect Cells,” in *MICCAI*. 2015, vol. 9351, pp. 276–283, Springer.
- [14] Y. Xie, F. Xing, X. Kong, H. Su, and L. Yang, “Beyond Classification: Structured Regression for Robust Cell Detection Using Convolutional Neural Network,” in *MICCAI*. 2015, vol. 9351, pp. 358–365, Springer.
- [15] R. Ferzli and L.J. Karam, “A No-Reference Objective Image Sharpness Metric Based on the Notion of Just Noticeable Blur (JNB),” *IEEE Trans. on Image Processing*, vol. 18, no. 4, pp. 717–728, Apr. 2009.
- [16] N. D. Narvekar and L. J. Karam, “A No-Reference Image Blur Metric Based on the Cumulative Probability of Blur Detection (CPBD),” *IEEE Trans. on Image Processing*, vol. 20, no. 9, pp. 2678–2683, Sept. 2011.
- [17] J. Guan, W. Zhang, J. Gu, and H. Ren, “No-reference blur assessment based on edge modeling,” *Journal of Visual Communication and Image Representation*, vol. 29, pp. 1–7, May 2015.
- [18] H. Wieslander et al., “Deep Convolutional Neural Networks for Detecting Cellular Changes Due to Malignancy,” in *2017 IEEE Int. Conf. on Computer Vision Workshops (ICCVW)*. Oct. 2017, pp. 82–89, IEEE.
- [19] O. Ronneberger, P. Fischer, and T. Brox, “U-Net: Convolutional Networks for Biomedical Image Segmentation,” in *MICCAI*. 2015, LNCS, pp. 234–241, Springer.
- [20] K. He, X. Zhang, S. Ren, and J. Sun, “Deep Residual Learning for Image Recognition,” *arXiv:1512.03385 [cs]*, Dec. 2015.
- [21] J. Jabalee, A. Carraro, T. Ng, E. Prisman, C. Garnis, and M. Guillaud, “Identification of malignancy-associated changes in histologically normal tumor-adjacent epithelium of patients with HPV-positive oropharyngeal cancer,” *Analytical Cellular Pathology*, vol. 2018, 2018.
- [22] C. Deroulers, D. Ameisen, M. Badoual, C. Gerin, A. Granier, and M. Lartaud, “Analyzing huge pathology images with open source software,” *Diagnostic Pathology*, vol. 8, no. 1, pp. 92, Dec. 2013.
- [23] S. Ioffe and C. Szegedy, “Batch normalization: Accelerating deep network training by reducing internal covariate shift,” *arXiv preprint arXiv:1502.03167*, 2015.
- [24] D.P. Kingma and J. Ba, “Adam: A Method for Stochastic Optimization,” *arXiv:1412.6980 [cs]*, Dec. 2014.